Automated Statistical Analysis of Raman Spectra of Nanomaterials

Natalia Martín Sabanés*, Matthew D. Eaton, Sara Moreno-Da Silva, Alicia Naranjo, Emilio M. Pérez*

IMDEA Nanoscience, C/ Faraday 9, 28049 Madrid

Abstract:

Both at the academic and the industrial level, material scientists are exploring routes for mass production and functionalization of graphene, carbon nanotubes (CNT), carbon dots, 2D materials, and heterostructures of these. Proper application of the novel materials requires fast and thorough characterization of the samples. Raman spectroscopy stands out as a standard non-invasive technique capable of giving key information on the structure and electronic properties of nanomaterials, including the presence of defects, degree of functionalization, diameter (in the case of CNT), different polytypes, doping, etc. Here, we present a computational tool to automatically analyze the Raman spectral features of nanomaterials, which we illustrate with the example of CNT and graphene. The algorithm manages hundreds of spectra simultaneously and provides statistical information (distribution of Raman shifts, average values of shifts and relative intensities, standard deviations, correlation between different peaks, etc.) of the main spectral features defining the structure and electronic properties of the samples, as well as publication-ready graphical material.

Introduction:

The field of nanoscience and nanotechnology has drawn extensive attention in the last decades due to the extraordinary physical and chemical properties of different materials in the nanoscale. The synthesis and development of nanomaterials and heterostructures of them is on high demand due their practical application at the academic and industrial level.[1,2] There are several types of nanomaterials, classified according to their dimensionality (from 0 to 2D) and their components (metal-based, semiconductors, nanocomposites, etc). One of the most common families of nanomaterials are the carbon-based nanomaterials,[3] with graphene, carbon nanotubes (CNT) or fullerenes as relevant examples. Material scientists are devoting their efforts to the development of advanced carbon-based nanomaterials taking advantage of the characteristics of the pristine material and using different doping methods to enhance properties for different applications.[4,5]

Examples of this and industrial applications can be found in many different fields, including composite fabrication,[6] (micro)electronics,[7–10] energy conversion devices,[11] biomedicine and health,[12,13] among others. Since the discovery of graphene and its extraordinary optical, electrical, mechanical and thermal properties, a variety of novel 2D materials have emerged trying to achieve similar characteristics with a sizable energy gap which will open the door to important applications in nanoelectronics.[14–17] Examples of these are the transition metal dichalcogenides family (TMDCs),[18] black phosphorus,[19] hexagonal boron nitride,[20] or metal-organic frameworks (MOFs).[21]

The mass production of nanomaterials for industrial use can result in heterogeneity within samples, with variations in size, doping levels, or diameters depending on the fabrication process, and with it comes a need for rapid and effective characterization to measure critical properties such as size, tube diameter, chiral angle, doping level, etc.[22–24] Raman spectroscopy has been established as a standard characterization tool to effectively characterize nanomaterials in a non-invasive manner both at ambient conditions and under controlled environments. With high energy resolution (down to the μeV regime), Raman is especially suitable for the characterization of specific nanomaterials such as the carbon-based and the TMDCs families due to highly efficient resonant effects which open the door to detect Raman inactive modes with enhanced sensitivity.[16,25–29]

After years of research, the Raman response of carbon-based materials is well understood and provides rich information about chemical composition, strain, doping and defects through the frequency shifts and intensity changes of their characteristic bands.[25,27,30] In particular, radial breathing modes (RBM ~50-350 cm^{-1}) are characteristic of NT and are related with their cylindrical shape. They are assigned to an out-of-plane bond stretching with frequency inversely proportional to the tube diameter.[31] The G band (~1584 cm^{-1}), an in-plane C-C bond stretching appears in all sp^2 carbon-based materials, and it splits in G$^+$ and G$^-$ peaks as a result of strain and electron-phonon coupling in CNT and uniaxially-stretched graphene. The D band (~1300-1400 cm^{-1}), also referred as defect mode, originates when the sp^2 network exhibits sp^3 defects. It is a double-resonance Raman peak that originates from the first order component of the hexagon-breathing mode (not active in first-order Raman scattering) combined with elastic scattering of an electron photoexcited by the defect. The 2D mode (~2600-2800 cm^{-1} also referred as G' by some authors)

is an overtone of the hexagon-breathing mode (forbidden in first-order Raman, but allowed as an overtone).[30]

Detailed analysis of the position and intensity changes of the described Raman bands gives information about the state of a given sample. For example, I_D/I_G ratio is directly proportional to the relative abundance of defects in the material,[32] so it has become a standard parameter to control defects and chemical doping induced by different fabrication methods. It is also an indicator of the degree of molecular covalent functionalization.[33,34] The linewidth and frequency of the D band can also be used to determine the degree of disorder in a material, and the coherence length.[32] The frequency of G and 2D bands is sensitive both to strain[35–37] and also to doping (both frequencies are extremely dependent on the extra charges induced by electrical and chemical methods).[38–40] By looking at the correlation between the Raman shifts of both modes (G and 2D), one can resolve the bimodal dependence on strain and charge doping effects of these two modes, and determine the type of doping based on the direction of the shifts (p- or n-).[41,42] Changes in temperature can also induce shifts of the G band, due to changes in the electron-phonon renormalization, phonon-phonon coupling and thermal expansion-induced volume changes.[43,44]

TMDCs are MX_2 layered structures (X-M-X trilayer with X= S, Se, Te and M= Mo, W, Nb) stacked by weak van der Waals forces.[45] Tailored materials can be designed by stacking TMDCs layers together with different energy band alignments and doping, achieving 2D heterostructures with specific properties. Raman spectroscopy emerges as a convenient tool for the characterization of TMDCs and their heterostructures, able to resolve the stacking characteristics between trilayers and their interactions.[29] The principal Raman active modes in TMDCs are: E_{2g}^1, an in-plane vibration where X and M atoms vibrate against each other; A_{1g}, out-of-plane vibration where the two X atoms within a trilayer vibrate in opposite directions; and B_{2g}, out-of-plane vibration where the X and M atoms within a trilayer vibrate against each other with a 180⁰ phase shift to the vibration in the adjacent layers.[28,46,47] E_{2g}^1 and A_{1g} undergo red and blue shifts, respectively, with increasing number of layers in MoS_2, WS_2, $MoSe_2$ and WSe_2, and hence their separation is a good indicator for material thickness.[29,48–50] Moreover, the evolution of both the linewidths and frequency shifts of these bands reflects the density of defects.[51] For heterostructures, the frequency difference between the main modes reflects the stoichiometry and stacking patterns[52],

and the B_{2g} mode is a fingerprint for interlayer coupling.[46] Additional second order peaks appear at certain materials under specific resonance conditions. For example, a broad spectral feature appears at 450 cm^{-1} in MoS$_2$, involving the longitudinal acoustic phonon at the M point (LA(M)) and has been used as a marker of flake functionalization.[53,54]

While detailed analysis of the Raman spectra of nanomaterials provides important information about the state of the sample, it requires mathematical treatment including baseline correction and fitting procedures for all interesting modes. This is easily doable to characterize one (or few) specific specimens, say a graphene or TMDC flake or a single CNT. A much more common situation when characterizing nanomaterials is that the sample is heterogeneous either chemically or physically, at least to some extent, so that typically hundreds of Raman spectra are acquired to get a representative picture of its properties. In these cases, detailed analysis of each individual spectrum becomes tedious and, in some cases, downright unfeasible. To overcome this, typically, researchers tend to provide the results for average spectra, reflecting the mean values of peak position and intensities over large amounts of material. However, the mean values fail to provide information of the heterogeneity within a sample, and small band shifts are often overlooked (and sometimes overinterpreted) given the spectral resolution of Raman spectrometers. In contrast, by analyzing the individual spectra obtained within a sample, the statistical distributions of spectral features can reveal important aspects of the nature of a material.

The evolution of programming languages and machine learning techniques in the last years have enabled the development of analysis routines that facilitate the extraction of relevant information of large-scale data. In this regard, different computational tools have been reported targeting the automatization of Raman analysis of nanomaterials. For instance, graphene thickness can be automatically inferred by analyzing the intensities of G and 2D modes in Raman mapping by Lorentzian fitting routines.[55] Principal component analysis (PCA)[56] has been introduced for the analysis and classification of large amount of Raman spectra of the carbon-based family.[57] For example, interlayer coupling and number of layers in graphene has been determined by means of parameterized PCA combined with neural-network.[58] Deep-learning techniques have been reported for automatic denoise of Raman spectra of graphene,[59] fit specific Raman bands and isolate the most informative Raman features to extract crystallinity or functionalization.[60] Similarly, the thickness of TMDCs and inhomogeneity can be automatically classified using neural

networks[61] and k-means clustering analysis,[62] respectively. These tools have been developed to meet specific user requirements, mostly related to the automatic assessment of material quality for industrial applications. To the best of our knowledge, a general tool targeting the spectral features (position, intensity and width) of all relevant Raman modes in the general case of nanomaterials has not been reported.

Here, we present a computational tool to automatically analyze the main Raman signatures of hundreds of spectra simultaneously, generalized for any type of nanomaterial. The algorithm analyzes single spectra separately and provides statistical distributions of the position, widths and intensity of the main Raman bands within a sample, instead of relying on the Raman response of the average spectrum, providing fitting errors and standard deviations for each parameter. It also allows the analysis of several samples simultaneously, such that the differences can be quickly spotted. Moreover, the user can plot Raman maps of specific spectral features, for samples where the spatial arrangement is relevant, such as in the case of controlled patterning of nanomaterials. This user-friendly code is available in MATLAB and Python programming languages. It is available as plain code to be used programmatically and modified according to needs by users with programming experience. A graphical user interface is also available for users without a programming background that simply want to use the code. In the following we discuss the code and its working principle including examples of results for single-walled CNT (SWNT), chemically modified SWNT samples and patterned graphene.

Methods:

a. Data analysis methodology:

The software allows to analyze a maximum of 10 different files (or samples) containing as many spectra per file as wanted. It is not required that all files contain the same number of spectra, however if the different files contain very different number of spectra, it is advisable to use the optional normalization feature, such that the generated histograms will be of comparable amplitude. The input files should be in .txt or .dat format, with a first column containing the wavenumber data (same for all spectra within a file) followed by intensity columns for each spectrum.

Each individual spectrum is initially normalized to the maximum of the peak defined by the user (normalization range defined by user as detailed in section b). Mathematically, the minimum value within a spectrum is subtracted from it (in order to account for unwanted constant baseline) and subsequently divided by the maximum value within the normalization range. A mean spectrum is calculated by averaging all normalized spectra within the same sample.

After normalization, the software calculates the spectral features of the main Raman signatures as defined by the user, in this example, those of carbon-based materials: RBM, D, G and 2D modes. Different analysis routines (for instance focusing on the E^1_{2g} and A_{1g} modes for 2H MoS_2) can be easily defined by the user. Note that currently, the code evaluates only 3 main Raman peaks, apart from the RBMs.

Method 1:

On one hand, a simple and fast analysis can be performed where the position of a certain band is defined as the wavenumber with maximum intensity within the band range specified by the user. As for the band height, it is calculated as the maximum intensity within a range minus the minimum intensity (figure 1). Intensity ratios are calculated by simply dividing the results from the intensities of the different modes. RBM modes are handled differently, due to the fact that several modes are expected in a small spectral range. To calculate peak position, we use the MATLAB function *findpeaks* (*scipy.signal.find_peaks* in Python) that locates local maxima within a vector. Position and height of each mode for each spectrum is stored and used to construct the population histograms returned by the software.

Note that this method does not perform proper band fitting, which will return the most accurate results and provide additional information such as the width of the peaks. However, the simple procedure described above allows for an important reduction of computation time, which is essential given that the algorithm is designed to handle large amount of data, and it works well provided that the raw data fulfill certain conditions. Specifically, irregular backgrounds result in mistakes in the calculation of position and intensity. For example, if a mode appears on a very steep linear background, and the selected spectral range contains portions of the background at higher intensity than the peak itself, the position and height will not be properly determined. This issue can be partially handled by selecting an appropriate spectral range or applying background correction routines before analysis. Advanced background correction routines are over the scope of this work and the reader is referred to the multiple tools available in literature if baseline correction is required for a specific set of data.[63-67] This method is recommended when a quick unsupervised analysis is desired, since the software can return accurate results for peak position and intensity with little input information from the user.

Method 2.1: Lorentzian fitting

The program can also evaluate the spectral features of the Raman modes performing proper peak fitting, if necessary. Spectral ranges selected by the user (see section b) are analyzed and Lorentzian band fitting is done following the expression:
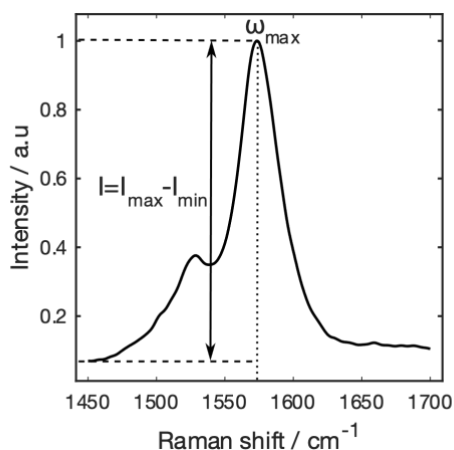

Figure 1: Scheme of the calculation of peak position and intensity for a Raman mode (the G band in a SWNT) with the method 1

$$y = y_0 + \frac{A}{(\omega - \omega_0)^2 + B} \tag{1}$$

Where ω is the wavenumber, y the intensity, and y_0, A, ω_0 and B are the fitting parameters. For a Lorentzian-shaped peak, ω_0 is the peak center, the full-width half maximum (FWHM) equals $2\sqrt{B}$, the maximum intensity at the peak center is A/B and y_0 is a constant value defining a baseline.

This method is more accurate at determining peak frequencies and it gives additional information such as the FWHM of the modes. In exchange, it requires a deeper supervision from the user to control the evolution of the fittings and it is, therefore, more dependent on the user defined inputs. In particular, the spectral range defined for each mode can alter the results. Generally speaking, the shorter range possible including the desired peak returns better results. In addition, this method requires the user defining initial estimates for the peak positions, intensities and FWHMs of each dataset analyzed. If the initial estimates are off, the fitting procedure might not converge and the analysis needs to be repeated. However, reasonable estimates for a given spectral feature of the nanomaterial under analysis are typically common knowledge. The fitting results are plotted such that the user can control the evolution of the analysis and repeat it selecting different spectral ranges and/or initial estimates. Moreover, as the method depends on the initial estimates, which are constant for a given dataset, it works fine when the spectral features within a sample are homogeneous. Drastic changes of background, peak position or intensity between spectra from a same sample, often results in inaccurate results, due to the fact that a set of initial guesses and spectral range cannot cover the variability within the sample. In these cases, it is preferable to use method 1. Alternatively, one can try to vary slightly the initial values repeating the analysis since often it is possible to find a set of estimates that work for all spectra within a sample. Note that RBM modes of CNT are not included in the Lorentzian fitting routine and are calculated in this case as explained previously.

In carbon-based nanomaterials, the G mode is split in two (G$^+$ and G$^-$) as a result of strain in CNT, or uniaxially stretched graphene. The software allows for the analysis of the G band as a double peak and the spectral features of G$^+$ and G$^-$ can be recovered independently. In this case, Lorentzian fitting as explained above is performed to the G spectral region, where 2 different peaks are located with 7 fitting parameters following the expression:

$$y = y_0 + \frac{A_{G+}}{\left(\omega - \omega_{0,G+}\right)^2 + B_{G+}} + \frac{A_{G-}}{\left(\omega - \omega_{0,G-}\right)^2 + B_{G-}} \tag{2}$$

The expression has one Lorentzian term for each of the peaks (G$^+$ and G$^-$), with the same parameters as described above and indicated with subscripts for each of the bands. Note that this split in two bands can be used with other Raman peaks when handling different nanomaterials. For example, when analyzing the A_{1g} mode in TMDCs, one can define a split to determine spectral features of the main peak and a commonly observed shoulder.

Method 2.2: Voigt fitting

A recent interlaboratory study has concluded that the standard deviation of peak widths of graphene spectra, especially for the 2D band, are substantially reduced if Voigt fitting is used instead of Lorentzian.[68] A Voigt function is a convolution of a Gaussian and a Lorentzian function and it captures better the broadening of the 2D mode resulting from doping, strain variations or increasing defect density since the gaussian component of the Voigt can accommodate the change in the peak tails. Therefore, we have developed an alternative code where Lorentzian fitting functions are replaced by a pseudo-Voigt functions as defined in OriginPro 2020 ('*PsdVoigt1*'):

$$y = y_0 + A[m_u \frac{2}{\pi} \frac{w}{4(x-x_0)^2 + w^2} + (1 - m_u)\frac{\sqrt{4ln2}}{\sqrt{\pi}w} e^{-\frac{4ln2}{w^2}(x-x_0)^2}] \tag{3}$$

where y_0 is a constant background, A is the peak area, w is the FWHM, x_0 is the peak center and m_u the profile shape-parameter (or gaussian weight/fraction).

Similar to the case of Lorentzian fitting, this method requires a supervised analysis by the user and the input of initial estimates for all the 5 fitting parameters. The output is dependent on the initial estimates and analysis needs to be repeated until the optimal settings (spectral ranges and initial estimates are found). The split of one of the peaks into 2 peaks (G$^+$ and G$^-$ in carbon-based materials) is also included in the Voigt fitting method, by just adding up two pseudo-Voigt functions as the one described in equation 3, with a single constant background (y_0).

Raman Mapping:

The statistical data and distributions of the spectral features of multiple measurements on a sample are very interesting when assuming the sample is homogenous over the measured region. However, sometimes samples are heterogenous, and differences in spectral features could be due to this sample heterogeneity and not statistical noise (for example the edges vs the

center of flakes). As such, mapping the spectra over the 2-dimensional area can give us important information about sample properties. The code has been developed to allow the user to map out selected spectral features over the measured area to help visualize these differences. Position of all Raman modes and intensity ratio between the main modes (I_D/I_G and I_{2D}/I_G for carbon-based materials) will be plotted in color maps. If Lorentzian (or Voigt fitting) is performed, Raman maps of the peak widths (FWHM) can also be generated. If several samples are analyzed simultaneously with the mapping option, the pixel numbers and dimensions need to be equal.

In addition, an interactive option is included in the Python code to help the user understand the spectral differences of the Raman maps. The code will save an image of a map of the selected feature for each file analyzed. However, only the last file analyzed can be further analyzed interactively. Using the matplotlib library in Python, pick event can be defined for clicking on a pixel of the final file's property map. Each pixel corresponds to a specific Raman spectrum. By clicking on a specific pixel, the code will open a new figure that plots the corresponding spectrum for that pixel. The *x* and *y* locations, as well as the chosen property's value will be listed in the legend, and a red dot is marked on the original property map on the selected pixels. Additional spectra can be added to the spectra plot by clicking on additional pixels on the map, and a text file containing all the spectra plotted in the figure will be updated with each click, as well as the saved image of the spectra graphic. By closing the spectra graph window, clicking on additional pixels on the map will clear the previously selected red dots and refresh the spectra plot as well as the output image and text file to only include the newly selected spectra.

b. User defined inputs:

The user is required to define certain parameters for the analysis. This can be done programmatically by modifying the first lines of code (notes are included in the code to guide the user about them), or interactively with a graphical user interface developed to facilitate the use to inexperience users. The required inputs are:

- File name(s), extension and path of the files to be analyzed. Also, the names for the legend of the generated plots have to be included. Note that the parameter 'total' is required and indicates the total number of files to be analyzed. The program will analyze

the number of files indicated in 'total' independently of the number of files specified in 'file_name'

- All spectra are normalized before further analysis, to the intensity maximum of a wavenumber range specified by the user as [normLow , normHigh].

- For the identification of peaks, the user has to include spectral regions where the signature peaks are located. In the case of RBM modes in CNT, a prominence value defining the maximum limit at which peaks will be considered is required. The prominence needs to be adjusted for each set of data, to account for variable noise and signal to noise ratio.

- If the analysis method 2 (Lorentzian fitting) is chosen, initial guesses for position, FWHM and maximum intensity of the Raman modes are required. For multiple file analysis, the user must define initial guesses for each of these files. If Voigt fitting is chosen, initial estimates for y_0, A, w, x_0 and m_u should be provided for each sample.

- If handling with a double G band, the analysis of G$^+$ and G$^-$ can be selected ('nt=1'), giving initial guesses for position, FWHM and maximum intensity of each of the peaks.

Additional inputs must be defined for using the mapping feature:

- A variable that defines whether the user wants to map the data.

- In the Python code, the user has to select which feature should be mapped. The user must input 'I' for intensity ratio, 'G' for G band, 'D' for D band, or '2D' for 2D band. The MATLAB code maps all peak positions and intensity ratios (and FWHM upon selection).

- Number of pixels in each column and row

- In python: Whether or not the user has the dimensions for the selected area. A value of 1 is used if the specific dimensions are used. If the value is 0, then the *x* and *y* axes will just be in units of pixel

- In MATLAB: The lengths of the *x* and *y* sides of the area in µm.

Last, the user can define to a certain extent the output plots generated by the program. In this way the computation time can be reduced by discarding certain plots according to user requirements. In particular, figures with raw data, normalized spectra, D, G and 2D spectral ranges selected by the user and RBM peak selection can be included or excluded. These figures

might be useful when first handling a new dataset in order to control the proper evolution of the analysis, but do not provide important information about the spectral features, and can be excluded at later stages. Moreover, the code allows plotting upon selection of certain correlations between spectral features.

c. Outputs:

The outputs of the program include figures and data. Regarding figures, the algorithm will return by default:

- Figure with the average spectrum for each of the samples analyzed, in the same graph.
- Histograms of the I_D/I_G and I_{2D}/I_G intensity ratio, and positions of the G (G^+ and G^-), D, 2D and RBM modes (in the general case I_2/I_1 and I_3/I_1 and position of peaks 1 (1+ and 1$^-$), 2 and 3). If several samples are analyzed simultaneously, the plots will include the results of each of them together in different colors. The average value and standard deviation for the specific feature are included in the figure legend. If the Lorentzian or Voigt fitting routines are chosen, figures with the distribution of FWHM for each peak will be also generated.
- Correlations between different spectral features: in this case, I_D/I_G vs G, D and 2D positions, 2D position vs G position and position vs FWHM of all modes. For each sample, and correlation, a linear fit is performed to the data and the resulting fitting function included in the legend. Note that any other correlation that might be needed can be easily included.

In addition, as described above, the user can include certain optional figures such as the raw and normalized spectra or the spectral ranges for each mode.

All results are also included in a .txt file saved automatically at the folder specified by path. A single file will be created for each different sample, including heights and positions of the G, D, 2D and RBM modes for each spectrum. In the case of Lorentzian or Voigt fittings, widths will also be included as well as the value of R^2 for each individual fitting to check the quality of the fit.

Results and discussion:

To illustrate the capabilities of the algorithm, we present the results obtained using this tool for the analysis and comparison of mechanically interlocked CNT (MINTs)[69–76] and the pristine 6,5-

SWNT used for their preparation. In particular, mechanical bonds are used to anchor Cu^{2+} metalloporphyrin dimeric rings around CNT to form magnetic cooper MINTs (Cu-mMINTs), as reported elsewhere.[77] The resulting Raman spectra are carefully analyzed in the following paragraphs.
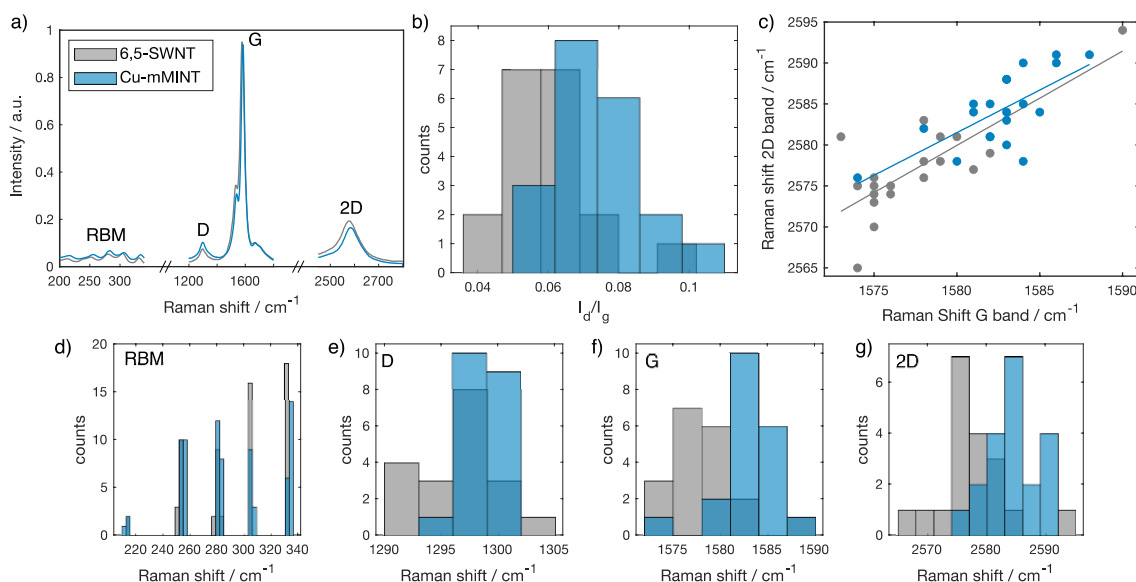

Figure 2: Results obtained applying method 1 for the comparison of 6,5-SWNT (gray) and Cu-mMINTs(blue). a) Raman spectra of Cu-mMINTs and the pristine 6,5-SWNT, corresponding to the average of 20 individual spectra. b) Distribution of the I_D/I_G ratio values obtained for each individual spectrum used to compose the average spectra in a; c) correlation between 2D and G Raman shifts. Distribution of Raman shifts of RBM (d), D (e), G (f) and 2D modes (g).

Cu-mMINTs and pristine SWNT are measured in a Senterra II Raman spectrometer, at 633 nm excitation wavelength and 10 mW power. 20 individual spectra are taken per sample. The average spectra for 6,5-SWNT and Cu-mMINTs are included in figure 2a. No notable differences between spectra are obvious from these data. Figure 2b, d-g include histograms summarizing the results for each individual spectrum of both samples: I_D/I_G ratio (Fig. 2b), peaks positions of RBM (Fig. 2d), D (Fig. 2e), G (Fig. 2f) and 2D (Fig. 2g) modes. Note that for this analysis the method 1 described in previous section was employed.

The I_D/I_G ratio is often used as a signature of the degree of defects induced in a material, and in this case can be used as an indicator of damage of the tubes as a consequence of the mMINT fabrication process. I_D/I_G goes from 0.06±0.01 to 0.08±0.01 in average for pristine and Cu-mMINT, respectively. The average values are therefore equal within error, which we interpret as no significant covalent functionalization during the formation of mMINTs. However, the histogram in figure 2b reflects a small but consistent increase of the I_D/I_G ratio during the mMINT reaction, assigned to the formation of a small number of defects while encapsulating the tubes with the

porphyrin rings due to the filtering, sonication and stirring steps. Although the total increase of the I_D/I_G ratio is small enough as to conclude that the overall structure of the tubes is mostly preserved upon mechanical interlocking, this analysis provides a much more complete picture of the chemical functionalization process.

Identical RBM modes are detected in both samples in terms of band position, indicating no notable change in the tube diameter upon the MINT fabrication process, as expected. However, a noticeable decrease in the relative intensity of the smaller diameter SWNTs (higher frequency Raman shift) is also observed. This is in line with our previous findings,[78] and reflects the diameter selectivity of the MINT formation reaction. A small blue shift of the 2D band in the Cu-mMINT (2585 cm^{-1}) with respect to the 6,5-SWNT (2578 cm^{-1}) is observed in the average spectra plotted in figure 2a, however the resolution of the spectrometer is 9 cm^{-1} and therefore, a shift of 7 cm^{-1} between two single spectra cannot be unambiguously assigned. In contrast, when looking at the statistical distribution of the position of the 2D mode among all individual spectra (figure 2g) the shift becomes more apparent, with two well defined and distinct spectral distributions. Similarly, a shift from 1577 cm^{-1} (6,5-SWNT) to 1583 cm^{-1} (Cu-mMINT) is observed in the G mode, and it is again reflected in the spectral distributions shown in figure 2f. Shifts of the G and 2D modes are usually good indicators of doping of the CNT due to the encapsulation but can also reflect strain. The correlation between the shifts of these modes can be used to disentangle the two effects.[41,42] Figure 2c includes a correlation between the shifts of the G and 2D modes, including a linear fit (solid lines) with slopes of 1.2±0.5 for the 6,5-SWNT and 1.0±0.5 for the Cu-mMINT sample. The slopes are almost identical within error for the tubes after encapsulation, which allows to discard
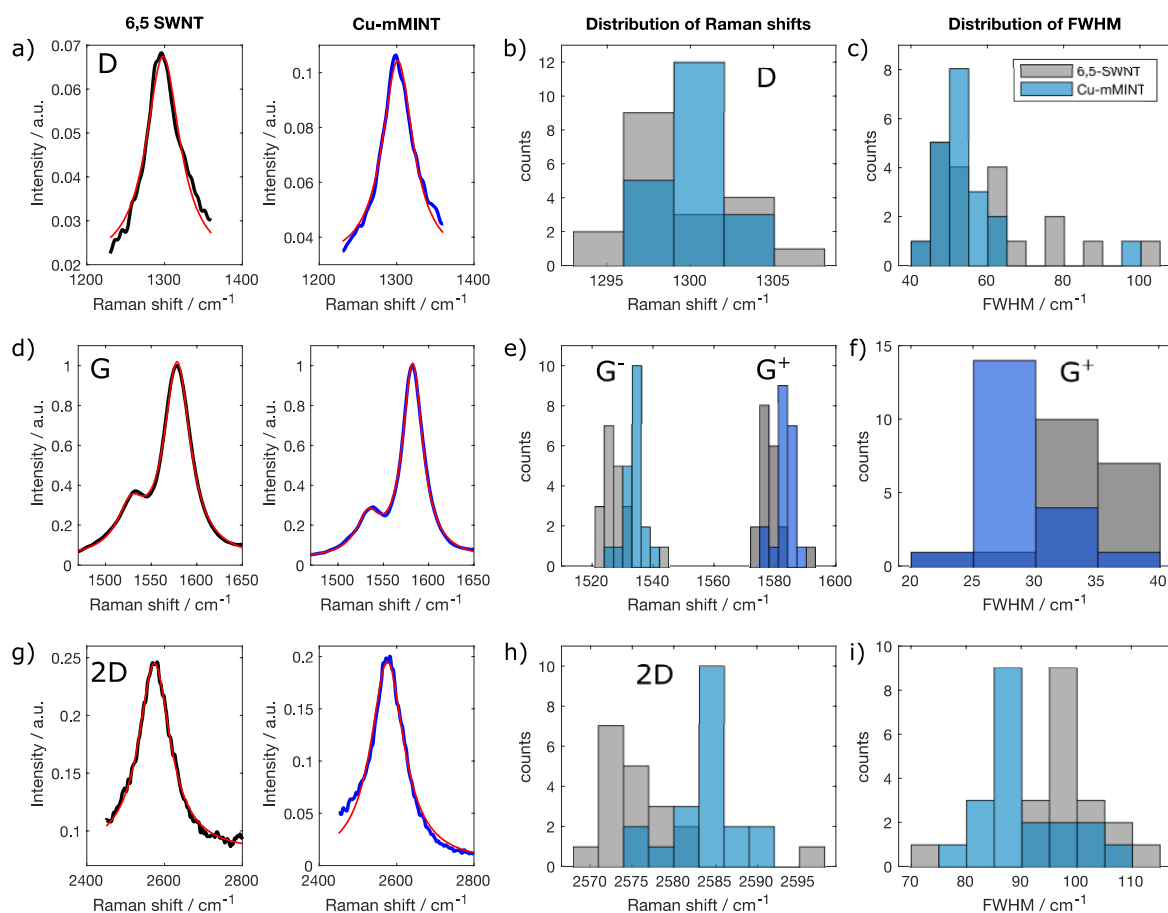
Figure 3: Analysis results obtained using Lorentzian peak fitting (method 2) for the same data reported in figure 2. Example of fittings for single spectra of 6,5-SWNT (black, left) and Cu-mMINTs (blue, right) in the D (a), G (d) and 2D (g) regions (in all cases the red curve represents the best fit to a Lorentzian, or double lorentzian function). The resulting histograms reflecting the distribution of Raman shifts and FWHM for all spectra within a sample are plotted in (b-c) for the D band; (e-f) for the G band split in G⁻ and G⁺ (only FWHM for the G⁺ band are plotted); and (h-i) for the 2D band. In all cases, 6,5-SWNTs are represented in gray and Cu-mMINTs in blue.

strong doping effects (significantly larger or smaller slopes will indicate p- or n-doping effects respectively),[42] confirming that the mMINT formation leads to no significant modulation of the electronic properties of the tubes, as we observed directly in the I/V characteristics of FET devices.[77]

Alternatively, we perform the analysis of the same datasets using method 2 (Lorentzian peak fitting), including the analysis of the G⁺ and G⁻ split. The results are included in figure 3, where example fittings, distribution of Raman shifts and distribution of FWHM are plotted for the D band (a-c), G band (d-f) and 2D band (g-i), for both 6,5-SWNT (gray) and Cu-mMINTs (blue). Numerical values for averaged position and FWHM of each band is included in table 1. The results obtained for band shifts are equivalent to the ones retrieved using method 1, with no shift of the D band (Fig. 3b), and small but noticeable blue shifts the 2D band (Fig. 3h and table 1) upon mMINT

formation. In the case of the G mode, this method allows resolving G^+ and G^- bands. Both G^+ and G^- present a small blue shift of 5 cm^{-1} (figure 3e and table 1).

The advantage of this method is that we can retrieve additional spectral features, such as the FWHM of the analyzed bands. We observe a decrease in the FWHM upon encapsulation of G^+ and 2D modes, as seen in figures 3f and i, respectively and summarized in table 1. Moreover, the FWHM is inversely proportional to the peak position for both modes, as shown in the correlations displayed in figure 4 c and d. The D band show a broad distribution of widths within each sample, as evident from the large errors for this mode in table 1, so a change cannot be unambiguously identified between samples. Sharpening of G mode has been observed as a result of doping in graphene[79,80] and CNT[81] (both electron and hole doping produce a decrease of FWHM) and attributed to blockage of the phonon decay into electro-hole pairs due to Pauli exclusion principle. The decrease of the FWHM of this peak is related with the blue shift of the mode as shown in Fig.4c and in agreement with previous reports.[79] While this is an indication of doping, the small magnitude of the shifts suggests that the doping effect is quantitatively very small. This observation is further supported by the linear distributions shown in figure 4b, relating the Raman shift of G and 2D modes. The slopes obtained for 6,5-SWNT and Cu-mMINTS are the same within error (1.4 ± 0.2 and 1.1 ± 0.3, respectively), thus strong doping effects are discarded, as concluded when using method 1. With respect to the intensity ratio I_D/I_G goes from 0.06 ± 0.01 to 0.07 ± 0.01 for pristine and Cu-mMINT tubes in average, respectively (Fig. 4a), showing a perfect agreement with the ratios obtained using method 1. The small increase evident in the distribution is attributed to the formation of small quantity of defects during the work up and purification processes, as explained above.

Table 1: Summary of averaged peak position and FWHM for each sample and mode using Lorentzian peak fitting

	Raman shift (cm^{-1})		FWHM (cm^{-1})	
	6,5-SWNT	Cu-mMINTs	6,5-SWNT	Cu-mMINTs

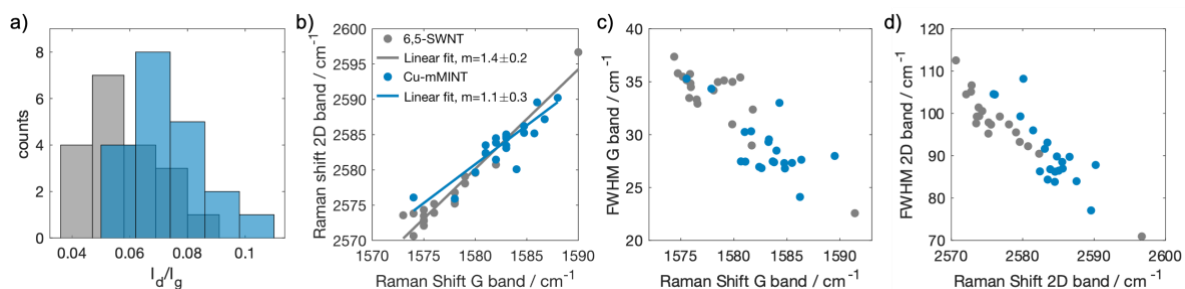|				
D	1300±3	1300±2	61±16	55±11
G⁻	1528±5	1533±3	35±5	33±3
G⁺	1578±4	1583±3	34±3	28±3
2D	2577±6	2584±4	98±8	91±8

Figure 4: a) Intensity ratio distribution of D and G bands; b) correlation between Raman shifts of 2D and G bands; c) correlation between FWHM and position of G band; and d) correlation between FWHM and position of 2D band for 6,5-SWNT and Cu-mMINTs in gray and blue, respectively, using analysis method 2.

In conclusion, the results of the analysis using both methods for these sets of data are almost identical, which validates the robustness of the simpler approach (method 1) to extract the relevant information regarding the Raman signature of the samples. Nevertheless, the peak fitting routine (method 2) is more precise and, in addition to peak position and intensity, returns a distribution of linewidths (FWHM) and correlations between all spectral features. Method 2 is therefore more complete and provides more detailed information about the samples which might be of interest for some users and applications.

Pseudo-Voigt peak fitting:

The results presented in figures 3 and 4 correspond to an analysis based on Lorentzian peak fitting. Our algorithm allows changing to pseudo-Voigt functions instead of Lorentzian. In figure 5 we present an example of the fitting of the 2D band of a graphene flake comparing the Lorentzian (eq.1) vs Voigt (eq. 3) fitting procedures.

Qualitatively, the Voigt function describes better the experimental data, especially the tales of the peak, where the Lorentz fit deviates and cannot describe perfectly the widening. However, both fitting functions retrieve almost identical values for the position (2676.1 cm⁻¹ for Lorentzian and

2676.0 cm^{-1} for Voigt) and intensity (1.07 a.u. for Lorentzian and 1.02 a.u for Voigt) of the peak. The FWHM values (25.7 cm^{-1} for Lorentzian and 28.1 cm^{-1} for Voigt) differ by 3 cm^{-1} and the R^2 value of the fittings are 0.9999 (Voigt) and 0.994 (Lorentz). Therefore, while the Voigt fitting describes better the widening of the peak in certain cases, the fitting results are almost identical using both methods

It is worth to mention that the fitting of a double peak using a double pseudo-Voigt function often fails to describe the experimental data, so in this case it is recommended to use the Lorentzian
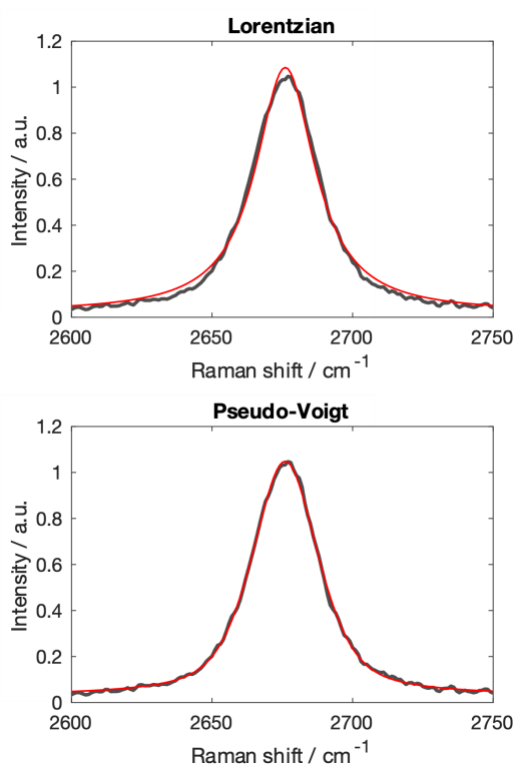

Figure 5: fitting of the 2D band in a single Raman spectrum from a graphene flake using a Lorentzian function (top) and pseudo-Voigt function.

fitting routine.

Mapping:

To demonstrate the mapping capability of the software, a 32 x 32 pixel map of I_D/I_G of a 38 μm x 42 μm region of patterned graphene is plotted in figure 6. This sample is a graphene substrate functionalized by a microemulsion pattering method consisting of 4-bromobenzenediazonium tetrafluoroborate dissolved in a microemulsion of water (+ T80 surfactant) and mineral oil.[33] The diazonium salt can functionalize the surface of graphene and dissolves better in water than oil. Covering the surface of graphene with the microemulsion results in small spherical regions of

non-functionalized surface, that correspond to the droplet sizes of the oil micelles where there is far less diazonium salt. This is evident from the spherical low I_D/I_G regions of the map in Fig. 6a, corresponding to the oil droplets. The functionalized regions have a much higher I_D/I_G value, as functionalization creates defects on the graphene sp^2 surface, leading to an increase in intensity of the D band.

The code allows the user to select and compare spectra from these two regions in an interactive manner. The selected pixels are marked with a red dot in Fig. 6a and the corresponding spectra are plotted in Fig. 6b with the low I_D/I_G, unfunctionalized region shown in blue vs. the high I_D/I_G, functionalized region in orange. The D band (1340 cm^{-1}) is clearly more intense in the patterned area than in the non-patterned region. This functionality within the code enables users to explore interactively their results.
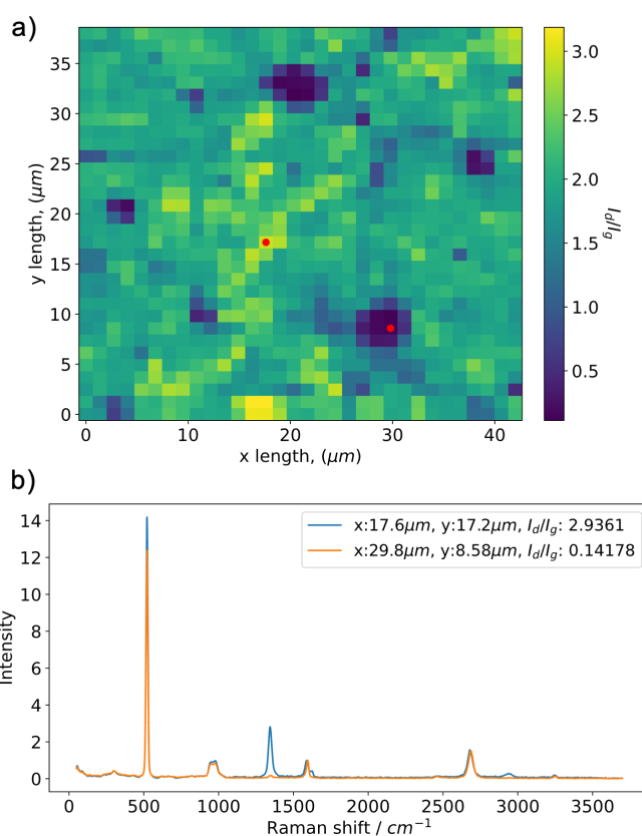

Figure 6: (a) Raman map of the D to G intensity ratio, I_D/I_G showing the patterning of a graphene substrate with an emulsion of diazonium salt. The darker areas correspond to unfunctionalized graphene. The red dots correspond to the location of the individual spectra plotted in (b).

Conclusions:

In conclusion, we present a user-friendly analysis routine that can be used by material scientists to extract all relevant information from their Raman spectra. The program is designed to handle large amount of data and analyze spectra individually, in a simple manner and with little supervision, while providing enough options for most users to obtain the useful information that will fully characterize any given material. The results include information about the fitting parameters for each individual spectrum analyzed, R^2 values for each fitting, average results for each spectral feature per file with the corresponding standard deviations. Moreover, the program generates figures including histograms for each parameter, correlations between spectral features and mappings. The required inputs from the user are spectral ranges for each Raman peak to be analyzed and initial estimates of the spectral features for the fittings (position, intensity and width). The code does not require to have extensive experience in Raman analysis or programming since it is designed to be easy to use and robust.

The analysis of spectral features can be performed using two different methods depending on user needs. Method 1 is based on finding local maxima within a spectrum, so it is simple yet it is still robust enough to provide band position and intensity pretty accurately. For a more detailed characterization, method 2 is suggested, where proper peak fitting is performed to recover also FWHM of the characteristic Raman bands. Both Lorentzian and Voigt fitting are available at the moment, depending on the characteristics of the spectra to handle. While Voigt fitting describes better the tales of broad peaks such as the 2D mode of graphene, Lorentz fitting works better when a double peak has to be fitted (such as the G split in carbon-based materials). Last, since it is the user that defines the spectral ranges where the peaks are located, the code can be easily adapted to analyze the Raman spectrum of any material by simply accommodating the spectral regions to the new sample. This will work fine for any 2D material, such as for example TMDCs.

Author Contributions:

N.M.S. designed and wrote the MATLAB codes, tested them on the different experimental datasets reported and wrote the manuscript. M.D.E. developed the Python codes and the interactive mapping option. S.M.dS and A.N. acquired the experimental data used in this work. E.M.P. assisted on the design and optimization of the codes and discussion of results. All authors contributed to the writing process.

Conflict of interest:

The authors have no conflicts to disclose

Data availability:

The codes and experimental data reported in this manuscript are openly available in IMDEA nanoscience repository (https://repositorio.imdeananociencia.org/handle/20.500.12614/3316).

References:

1.   Baig, N., Kammakakam, I., Falath, W. & Kammakakam, I. Nanomaterials: A review of synthesis methods, properties, recent progress, and challenges. *Mater. Adv.* **2**, 1821–1871 (2021).

2.   Kolahalam, L. A. *et al.* Review on nanomaterials: Synthesis and applications. *Mater. Today Proc.* **18**, 2182–2190 (2019).

3.   Ferrari, A. C. *et al.* Science and technology roadmap for graphene, related two-dimensional crystals, and hybrid systems. *Nanoscale* **7**, 4598–4810 (2015).

4.   Barkan, T. Graphene: the hype versus commercial reality. *Nat. Nanotechnol.* **14**, 904–906 (2019).

5.   Ye, R. & Tour, J. M. Graphene at fifteen. *ACS Nano* **13**, 10872–10878 (2019).

6.   Coleman, J. N., Khan, U., Blau, W. J. & Gun'ko, Y. K. Small but strong: A review of the mechanical properties of carbon nanotube-polymer composites. *Carbon N. Y.* **44**, 1624–1652 (2006).

7.   Peng, L. M., Zhang, Z. & Wang, S. Carbon nanotube electronics: Recent advances.

Mater. Today **17**, 433–442 (2014).

8. Hoenlein, W. *et al.* Carbon nanotube applications in microelectronics. *IEEE Trans. Components Packag. Technol.* **27**, 629–634 (2004).

9. Wei, Z. *et al.* Nanoscale Tunable Reduction of Graphene Oxide for Graphene Electronics. *Science (80-.).* **328**, 1373–1376 (2010).

10. Bonaccorso, F., Sun, Z., Hasan, T. & Ferrari, A. C. Graphene photonics and optoelectronics. *Nat. Photonics* **4**, 611–622 (2010).

11. Tune, D. D., Flavel, B. S., Krupke, R. & Shapter, J. G. Carbon nanotube-silicon solar cells. *Adv. Energy Mater.* **2**, 1043–1055 (2012).

12. Bianco, A., Kostarelos, K., Partidos, C. D. & Prato, M. Biomedical applications of functionalised carbon nanotubes. *Chem. Commun.* 571–577 (2005). doi:10.1039/b410943k

13. Jorio, A. *Bioengineering Applications of Carbon Nanostructures.* (Springer, 2016). doi:10.1016/b978-012221820-0/50020-4

14. Hu, Z. *et al.* Two-dimensional transition metal dichalcogenides: Interface and defect engineering. *Chem. Soc. Rev.* **47**, 3100–3128 (2018).

15. Wang, S., Pratama, F. R., Ukhtary, M. S. & Saito, R. Independent degrees of freedom in two-dimensional materials. *Phys. Rev. B* **101**, 1–5 (2020).

16. Niranjan, M. K., Karthik, T., Asthana, S., Pan, J. & Waghmare, U. V. Theoretical and experimental investigation of Raman modes, ferroelectric and dielectric properties of relaxor Na0.5Bi0.5TiO 3. *J. Appl. Phys.* **113**, 0–7 (2013).

17. Paul, J., Nishimatsu, T., Kawazoe, Y. & Waghmare, U. V. A first-principles study of phase transitions in ultrathin films of BaTiO3. *Pramana - J. Phys.* **70**, 263–270 (2008).

18. Lopez-Sanchez, O., Lembke, D., Kayci, M., Radenovic, A. & Kis, A. Ultrasensitive photodetectors based on monolayer MoS 2. *Nat. Nanotechnol.* **8**, 497–501 (2013).

19. Ling, X., Wang, H., Huang, S., Xia, F. & Dresselhaus, M. S. The renaissance of black phosphorus. *Proc. Natl. Acad. Sci. U. S. A.* **112**, 4523–4530 (2015).

20. Kubota, Y., Watanabe, K., Tsuda, O. & Taniguchi, T. Deep Ultraviolet Light–Emitting Hexagonal Boron Nitride Synthesized at Atmospheric Pressure. *Science (80-.).* **317**, 932–935 (2007).

21. Usman, M., Mendiratta, S. & Lu, K. L. Semiconductor Metal–Organic Frameworks: Future Low-Bandgap Materials. *Adv. Mater.* **29**, 1605071 (2017).

22. Kovtun, A. *et al.* Benchmarking of graphene-based materials: Real commercial products versus ideal graphene. *2D Mater.* **6**, 025006 (2019).

23. Clifford, C. A. *et al.* The importance of international standards for the graphene community. *Nat. Rev. Phys.* **3**, 233–235 (2021).

24. Pollard, A. J. Metrology for graphene and 2D materials. *Meas. Sci. Technol.* **27**, 092001 (2016).

25. Wu, J. Bin, Lin, M. L., Cong, X., Liu, H. N. & Tan, P. H. Raman spectroscopy of graphene-based materials and its applications in related devices. *Chem. Soc. Rev.* **47**, 1822–1873 (2018).

26. Malard, L. M., Pimenta, M. A., Dresselhaus, G. & Dresselhaus, M. S. Raman spectroscopy in graphene. *Phys. Rep.* **473**, 51–87 (2009).

27. Ferrari, A. C. & Basko, D. M. Raman spectroscopy as a versatile tool for studying the properties of graphene. *Nat. Nanotechnol.* **8**, 235–246 (2013).

28. Fan, J. H. *et al.* Resonance Raman scattering in bulk 2H-MX2 (M = Mo, W; X = S, Se) and monolayer MoS2. *J. Appl. Phys.* **115**, 053527 (2014).

29. Saito, R., Tatsumi, Y., Huang, S., Ling, X. & Dresselhaus, M. S. Raman spectroscopy of transition metal dichalcogenides. *J. Phys. Condens. Matter* **28**, 353002 (2016).

30. Jorio, A., Saito, R., Dresselhaus, G. & Dresselhaus, M. S. *Raman Spectroscopy in Graphene Related Systems*. (Wiley-VCH, 2011).

31. Jorio, A. & Saito, R. Raman spectroscopy for carbon nanotube applications. *J. Appl. Phys.* **129**, (2021).

32. Lucchese, M. M. *et al.* Quantifying ion-induced defects and Raman relaxation length in

graphene. *Carbon N. Y.* **48**, 1592–1597 (2010).

33.   Naranjo, A., Sabanés, N. M., Sulleiro, M. V. & Pérez, E. M. Microemulsions for the covalent patterning of graphene. *Chem. Commun.* **58**, 7813–7816 (2022).

34.   Criado, A., Melchionna, M., Marchesan, S. & Prato, M. The Covalent Functionalization of Graphene on Substrates. *Angew. Chemie - Int. Ed.* **54**, 10734–10750 (2015).

35.   Huang, M. *et al.* Phonon softening and crystallographic orientation of strained graphene studied by Raman spectroscopy. *Proc. Natl. Acad. Sci. U. S. A.* **106**, 7304–7308 (2009).

36.   Metzger, C. *et al.* Biaxial strain in graphene adhered to shallow depressions. *Nano Lett.* **10**, 6–10 (2010).

37.   Yoon, D., Son, Y. W. & Cheong, H. Strain-dependent splitting of the double-resonance raman scattering band in graphene. *Phys. Rev. Lett.* **106**, 1–4 (2011).

38.   Yan, J., Zhang, Y., Kim, P. & Pinczuk, A. Electric field effect tuning of electron-phonon coupling in graphene. *Phys. Rev. Lett.* **98**, 1–4 (2007).

39.   Ryu, S. *et al.* Atmospheric oxygen binding and hole doping in deformed graphene on a SiO2 substrate. *Nano Lett.* **10**, 4944–4951 (2010).

40.   Berciaud, S., Ryu, S., Brus, L. E. & Heinz, T. F. Probing the Intrinsic Properties of Exfoliated Graphene: Raman Spectroscopy of Free-Standing Monolayers. *Nano Lett.* **9**, 346–352 (2009).

41.   Lee, J. E., Ahn, G., Shim, J., Lee, Y. S. & Ryu, S. Optical separation of mechanical strain from charge doping in graphene. *Nat. Commun.* **3**, 1024–1028 (2012).

42.   Blanco, M. *et al.* Positive and negative regulation of carbon nanotube catalysts through encapsulation within macrocycles. *Nat. Commun.* **9**, 1–7 (2018).

43.   Calizo, I., Balandin, A. A., Bao, W., Miao, F. & Lau, C. N. Temperature dependence of the raman spectra of graphene and graphene multilayers. *Nano Lett.* **7**, 2645–2649 (2007).

44.   Raravikar, N. R. *et al.* Temperature dependence of radial breathing mode Raman frequency of single-walled carbon nanotubes. *Phys. Rev. B - Condens. Matter Mater.*

Phys. **66**, 1–9 (2002).

45.   Wang, S., Ukhtary, M. S. & Saito, R. Strain effect on circularly polarized electroluminescence in transition metal dichalcogenides. *Phys. Rev. Res.* **2**, 1–7 (2020).

46.   Pan, Y. & Zahn, D. R. T. Raman Fingerprint of Interlayer Coupling in 2D TMDCs. *Nanomaterials* **12**, 1–10 (2022).

47.   Molina-Sánchez, A. & Wirtz, L. Phonons in single-layer and few-layer MoS2 and WS2. *Phys. Rev. B - Condens. Matter Mater. Phys.* **84**, 1–8 (2011).

48.   Quirós-Ovies, R. *et al.* Microwave-Driven Exfoliation of Bulk 2H-MoS 2 after Acetonitrile Prewetting Produces Large-Area Ultrathin Flakes with Exceptionally High Yield. *ACS Nano* **17**, 5984–5993 (2023).

49.   Yamamoto, M. *et al.* Strong enhancement of Raman scattering from a bulk-inactive vibrational mode in few-layer MoTe2. *ACS Nano* **8**, 3895–3903 (2014).

50.   Li, H. *et al.* From bulk to monolayer MoS 2: Evolution of Raman scattering. *Adv. Funct. Mater.* **22**, 1385–1390 (2012).

51.   Mignuzzi, S. *et al.* Effect of disorder on Raman scattering of single-layer Mo S2. *Phys. Rev. B - Condens. Matter Mater. Phys.* **91**, 1–7 (2015).

52.   Liang, L. & Meunier, V. First-principles Raman spectra of MoS2, WS2 and their heterostructures. *Nanoscale* **6**, 5394–5401 (2014).

53.   Knirsch, K. C. *et al.* Basal-Plane Functionalization of Chemically Exfoliated Molybdenum Disulfide by Diazonium Salts. *ACS Nano* **9**, 6018–6030 (2015).

54.   Sulleiro, M. V. *et al.* Fabrication of devices featuring covalently linked MoS2–graphene heterostructures. *Nat. Chem.* **14**, 695–700 (2022).

55.   Caridad, J. M., Rossella, F., Bellani, V., Grandi, M. S. & Diez, E. Automated detection and characterization of graphene and few-layer graphite via Raman spectroscopy. *J. Raman Spectrosc.* **42**, 286–293 (2011).

56.   Jolliffe, I. T. *Principal Component Analysis.* (Springer-Verlag, 2002).

57.   Campos, J. L. E. *et al.* Applications of Raman spectroscopy in graphene-related

materials and the development of parameterized PCA for large-scale data analysis. *J. Raman Spectrosc.* **49**, 54–65 (2018).

58. Silva, D. L. *et al.* Raman spectroscopy analysis of number of layers in mass-produced graphene flakes. *Carbon N. Y.* **161**, 181–189 (2020).

59. Machado, L. R. P. *et al.* Deep-learning-based denoising approach to enhance Raman spectroscopy in mass-produced graphene. *J. Raman Spectrosc.* **53**, 863–871 (2022).

60. Orts Mercadillo, V., Ijije, H., Chaplin, L., Kinloch, I. A. & Bissett, M. A. Novel techniques for characterising graphene nanoplatelets using Raman spectroscopy and machine learning. *2D Mater.* **10**, (2023).

61. Aleithan, S. H. & Mahmoud-Ghoneim, D. Toward automated classification of monolayer versus few-layer nanomaterials using texture analysis and neural networks. *Sci. Rep.* **10**, 1–8 (2020).

62. Xin, H., Zhang, J., Yang, C. & Chen, Y. Direct Detection of Inhomogeneity in CVD-Grown 2D TMD Materials via K-Means Clustering Raman Analysis. *Nanomaterials* **12**, (2022).

63. He, S. *et al.* Baseline correction for Raman spectra using an improved asymmetric least squares method. *Anal. Methods* **6**, 4402–4407 (2014).

64. Guo, S., Bocklitz, T. & Popp, J. Optimization of Raman-spectrum baseline correction in biological application. *Analyst* **141**, 2396–2404 (2016).

65. Liu, H. *et al.* Joint baseline-correction and denoising for raman spectra. *Appl. Spectrosc.* **69**, 1013–1022 (2015).

66. Korepanov, V. I. Asymmetric least-squares baseline algorithm with peak screening for automatic processing of the Raman spectra. *J. Raman Spectrosc.* **51**, 2061–2065 (2020).

67. Zhao, J., Lui, H., Mclean, D. I. & Zeng, H. Automated autofluorescence background subtraction algorithm for biomedical raman spectroscopy. *Appl. Spectrosc.* **61**, 1225–1232 (2007).

68. Turner, P. *et al.* International interlaboratory comparison of Raman spectroscopic

analysis of CVD-grown graphene. *2D Mater.* **9**, (2022).

69.   Pérez, E. M. Putting Rings around Carbon Nanotubes. *Chem. - A Eur. J.* **23**, 12681–12689 (2017).

70.   Miki, K. *et al.* Unique Tube–Ring Interactions: Complexation of Single-Walled Carbon Nanotubes with Cycloparaphenyleneacetylenes. *Small* **14**, 1–9 (2018).

71.   López-Moreno, A., Villalva, J. & Pérez, E. M. Mechanically interlocked derivatives of carbon nanotubes: synthesis and potential applications. *Chem. Soc. Rev.* **51**, 9433–9444 (2022).

72.   De Juan, A. *et al.* Mechanically interlocked single-wall carbon nanotubes. *Angew. Chemie - Int. Ed.* **53**, 5394–5400 (2014).

73.   Cheng, G. *et al.* Interlocking of Single-Walled Carbon Nanotubes with Metal-Tethered Tetragonal Nanobrackets to Enrich a Few Hundredths of a Nanometer Range in Their Diameters. *ACS Nano* **16**, 12500−12510 (2022).

74.   López-moreno, A. *et al.* Single-Walled Carbon Nanotubes Encapsulated within Metallacycles Angewandte. *Angew. Chemie Int. Ed.* **61**, e202208189 (2022).

75.   De Juan-Fernández, L. *et al.* Interfacing porphyrins and carbon nanotubes through mechanical links. *Chem. Sci.* **9**, 6779–6784 (2018).

76.   Balakrishna, B. *et al.* Dynamic Covalent Formation of Concave Disulfide Macrocycles Mechanically Interlocked with Single-Walled Carbon Nanotubes. *Angew. Chemie - Int. Ed.* **59**, 18774–18785 (2020).

77.   Moreno-Da Silva, S. *et al.* Magnetic, Mechanically Interlocked Porphyrin-Carbon Nanotubes for Quantum Computation and Spintronics. *J. Am. Chem. Soc.* **143**, 21286–21293 (2021).

78.   Martínez-Periñán, E. *et al.* The mechanical bond on carbon nanotubes: Diameter-selective functionalization and effects on physical properties. *Nanoscale* **8**, 9254–9264 (2016).

79.   Casiraghi, C., Pisana, S., Novoselov, K. S., Geim, A. K. & Ferrari, A. C. Raman fingerprint of charged impurities in graphene. *Appl. Phys. Lett.* **91**, 1–4 (2007).

80. Pisana, S. *et al.* Breakdown of the adiabatic Born-Oppenheimer approximation in graphene. *Nat. Mater.* **6**, 198–201 (2007).

81. Wu, Y. *et al.* Variable electron-phonon coupling in isolated metallic carbon nanotubes observed by Raman scattering. *Phys. Rev. Lett.* **99**, 1–4 (2007).